
Auto-WHATMD : Automated Wasserstein-based High-dimensional feature extraction Analysis of Trajectories from Molecular Dynamics

Sosuke Asano¹ Ikki Yasuda¹ Katsuhiro Endo² Yoshinori Hirano¹ Kenji Yasuoka¹

Abstract

Comparing multiple protein systems with variation such as different binding ligands or mutations, and understanding their effects is one of the objectives in molecular dynamics simulations. Representation of these systems by a few features enables quantitative comparison. However, because molecular dynamics simulation trajectories are high-dimensional spatiotemporal data, selection of key features relies on domain expertise, sometimes introducing arbitrary assumptions. Here, we present an approach that uses the optimal transport distance to compare high-dimensional trajectory data, and employs simulated annealing to identify the residues that best distinguish multiple systems. We term this algorithm auto-WHATMD (automated Wasserstein-based High-dimensional feature extraction Analysis for Trajectories of Molecular Dynamics). We applied auto-WHATMD to multiple protein-ligand systems of bromodomain 4 with different ligands, identifying the most discriminative residues in the loop region. Moreover, even a few selected residues were sufficient to capture the correlation with ligand-binding affinities, indicating that auto-WHATMD effectively prioritizes the most informative residues. Our approach can be used to efficiently determine key residues and design features for multiple analogous systems.

1. Introduction

Proteins have unique structures and dynamics with specific amino acid sequences. These structural and dynamic features are critical for their biological functions, including special tertiary structures that function as catalytic sites

¹Department of Mechanical Engineering, Keio University, Yokohama, Kanagawa, Japan ²National Institute of Advanced Industrial Science and Technology, Tsukuba, Ibaraki, Japan. Correspondence to: Kenji Yasuoka <yasuoka@mech.keio.ac.jp>.

and ligand recognition sites or selective ion and ligand-dependent channels (Karplus & Kuriyan, 2005), as well as flexible disordered regions that recognize other proteins and regulate self-assembly behaviors (Van Der Lee et al., 2014). However, many proteins have heterogeneous conformations, including metastable structures, in addition to the single structure accessible from X-ray crystal structure analysis data and prediction from machine learning models (Bottaro & Lindorff-Larsen, 2018). This heterogeneity can range from minor scale, such as side-chain orientation change, to major-scale conformational changes, including open and close loop protein transitions (Henzler-Wildman & Kern, 2007).

Computational approaches for studying protein structural ensembles have been developed based on either physics-based methods, data-driven methods, or a combination of both. Molecular dynamics (MD) simulations, often starting from crystal structures, can capture structural changes and dynamics at atomistic or molecular resolution. They are widely employed to investigate protein dynamics and to sample heterogeneous conformational ensembles, providing valuable insights into protein folding, conformational changes, and ligand binding (Lindorff-Larsen et al., 2011; Plattner & Noé, 2015). Recently, machine learning approaches have been developed to predict static structures such as AlphaFold and similar methods (Jumper et al., 2021; Baek et al., 2021) and further being extending to prediction of conformational ensembles (Lewis et al., 2025). These methods include generative models such as flow-based models (Noé et al., 2019), generative adversarial networks (Janson et al., 2023), and diffusion models (Lu et al., 2024; Lewis et al., 2024).

Comparing structural ensembles is an important but challenging task (Vögele et al., 2025). For evaluating a single structure, commonly employed approaches include contact maps, root mean square deviation (RMSD), t-SNE and relevant physical quantities (Mardt et al., 2018; Lemke & Peter, 2019; Glielmo et al., 2021). Comparing ensembles is more challenging because they represent distributions of conformations rather than individual structures. Further, molecular dynamics ensembles are generally time series of conformations, and therefore the ensemble is characterized by structural and temporal aspects, such as relaxation dynam-

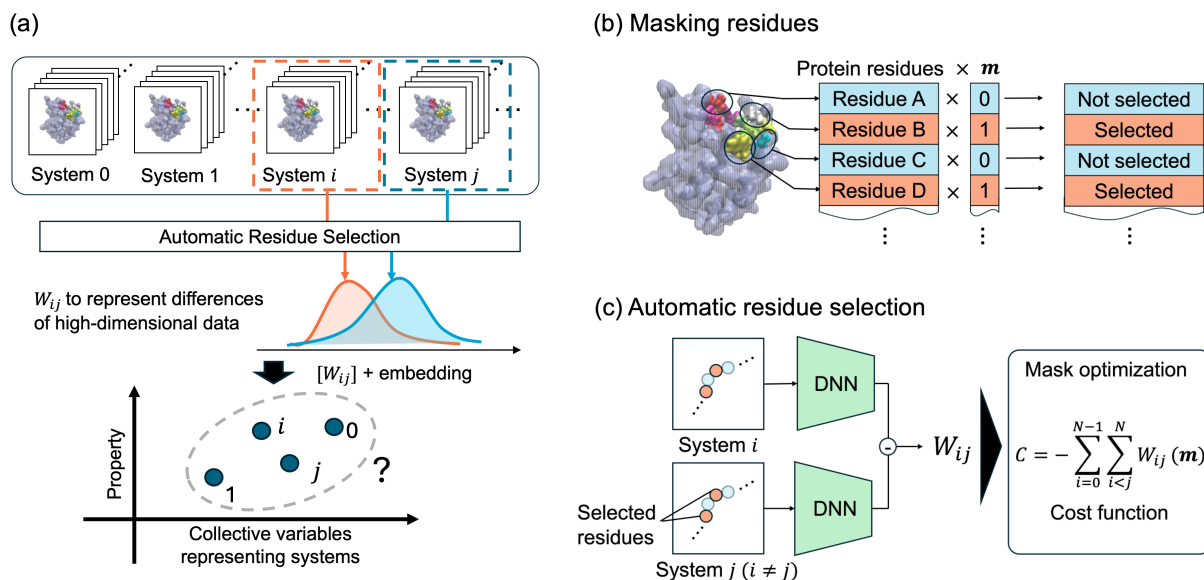


Figure 1. Schematic overview of auto-WHATMD. (a) Multiple systems are prepared and important residues are automatically selected from the entire protein. Trajectories of the selected residues are represented as high-dimensional data distributions. Differences between systems are quantified using the Wasserstein distance, and the resulting distance matrix is embedded into a low-dimensional space to analyze relationships between collective variables and system properties. (b) Important residues selected from the protein are indicated by residue masking. (c) Optimization for automatic residue selection. System differences computed by a deep neural network are used to optimize the mask vector.

ics and diffusion (Endo et al., 2018). This motivates the need for systematic and objective methods to quantitatively compare conformational ensembles.

Optimal transport-based approaches have been developed and validated for comparing ensembles of biomolecules derived from MD simulations (Endo et al., 2019; Yasuda et al., 2022; González-Delgado et al., 2023; Mustali et al., 2023), alongside other comparison metrics (also see Related Work). However, feature selection plays a critical role in characterizing ensembles, as it significantly affects their representations. Trial and error is often required to achieve the desired representation; otherwise, inappropriate feature selection can lead to misleading interpretations.

In this work, we present a method for automatically selecting representative amino acid residues from the protein, and thereby comparing ensembles of multiple analogous systems. We applied this method to protein-ligand systems of a benchmarking protein bromodomain 4 (BRD4), using different ligand species bound to the protein. We demonstrated that our approach enables the successful identification of the crucial binding-site residues, and the differences in selected residues are associated with ligand-binding affinity.

2. Related Work

As a pioneering work in ensemble comparison, Brüschweiler extended the concept of RMSD to con-

formational ensembles and proposed the inter-ensemble RMSD (eRMSD) (Brüschweiler, 2003). While this approach is both simple and useful, it has several limitations. For example, the eRMSD within the same ensemble is not zero and higher-order moments beyond the second moment are not considered. Consequently, it cannot fully capture the complexity of ensemble distributions. Lindorff-Larsen et al. assumed that MD ensembles are sampled from the ground-truth distributions approximated as the sum of Gaussians (Lindorff-Larsen & Ferkinghoff-Borg, 2009; Tiberti et al., 2015). They estimated these ensemble distributions and then computed metrics for comparison such as the Kullback-Leibler or Jensen-Shannon divergence. By applying dimensionality reduction to these matrices and projection onto 2D space, they further compared structural ensembles obtained from different experimental methodologies and MD simulation force fields (Lindorff-Larsen & Ferkinghoff-Borg, 2009). González-Delgado et al. utilized the Wasserstein distance (González-Delgado et al., 2023), which satisfies the axioms of a distance matrix and does not require any assumptions about the ground-truth distribution. They computed the Wasserstein distance for one-dimensional distributions of properties, such as the residue-residue distances and radius of gyration of disordered proteins, and demonstrated that it can differentiate conformational ensembles.

Yasuda et al. proposed that the conformation dynamics of

proteins are represented by an ensemble of short-term trajectories sampled from long MD trajectories, and that differences between two such ensembles can be quantified using the Wasserstein distance (Endo et al., 2019; Yasuda et al., 2022). Since the Wasserstein distance for high-dimensional distributions cannot be computed using linear algorithms due to its high computational cost (Villani et al., 2009), they approximated it using neural networks (Arjovsky et al., 2017; Endo et al., 2019). They demonstrated that multiple protein-ligand systems, differing only in ligand species, are projected into a feature space that correlates with binding affinity. However, this approach assumes that the systems are represented by a specific set of residues selected before computing the Wasserstein distance, which may introduce bias due to the potentially arbitrary choice of residues.

3. Proposed Method

Auto-WHATMD automatically performs feature extraction to differentiate multiple analogous systems, comprising three steps (Fig. 1a): quantification of pairwise system differences based on the Wasserstein distance, automatic residue selection, and low-dimensional representation of the system differences. Previously, up to 20 residues were manually selected as input, ideally avoiding irrelevant residues (Yasuda et al., 2022). Auto-WHATMD automates this selection process, enabling automated analysis of multiple analogous systems.

We represent residue selection using a binary mask vector (Fig. 1b), which indicates that the residue is included as input, and not included otherwise. Thus, the problem of residue selection is addressed by optimizing the mask vector. In the following sections, we present the methods to quantify the system differences, the optimization procedure of the mask, and a method to represent the pairwise system differences in low dimensions.

3.1. Training neural network to calculate Wasserstein distance

Wasserstein distance is used as a measurement of distance between two distributions (Villani et al., 2009), herein we use it to measure differences of two MD ensembles. For low-dimensional distributions, the Wasserstein distance can be calculated using linear programming with moderate computational cost. However, such methods are not feasible for high-dimensional distributions of short-time dynamics. Recently, neural networks have been used to approximate the Wasserstein distance in generative adversarial networks (Arjovsky et al., 2017).

We regard an MD system as a single distribution of high-dimensional data, referred to as the local dynamics en-

semble, which consists of samples of short-term trajectories (Endo et al., 2019). The local dynamics ensemble is useful for representing time-series data of many-particle systems in a data size suitable for neural network architectures. One sample from the local dynamics ensemble has a dimensionality equal to the product of three factors (the time steps of the local dynamics, the number of selected residues, and the number of dimensions, which is three in xyz space).

When the input is masked by a binary vector, the Wasserstein distance between the two local dynamics ensembles is defined as,

$$W_{ij}(\mathbf{m}) = \sup_{\|f_{ij}\|_L \leq 1} \mathbb{E}_{\mathbf{x}_i \sim \mathbf{y}_i} [f_{ij}(\mathbf{m} \odot \mathbf{x}_i)] - \mathbb{E}_{\mathbf{x}_j \sim \mathbf{y}_j} [f_{ij}(\mathbf{m} \odot \mathbf{x}_j)] \quad (1)$$

where f_{ij} is a critic function represented by a deep neural network, and $\sup_{\|f_{ij}\|_L \leq 1}$ denotes the maximization over the space of functions satisfying the 1-Lipschitz constraint, \mathbb{E} is the expectation, and \mathbf{x}_i is the data sampled from the distribution of local dynamics ensemble of system i , denoted by \mathbf{y}_i . The input data \mathbf{x}_i is masked using the binary vector, \mathbf{m} , \mathbf{m}_t and \mathbf{m}_{new} are used to mask the input data. For simplicity, they are collectively represented as \mathbf{m} in this explanation.

The neural network function, f_{ij} , is trained for a specific pair of the local dynamics ensembles of interest. However, the mask is not yet determined at this stage of optimization of f_{ij} , and thus the local dynamics ensembles of residues to be selected are also not determined. To address this, we randomly generate binary mask vectors for each step of training f_{ij} , under the assumption that f_{ij} can output an approximation of the Wasserstein distance for varying mask vectors.

To satisfy the 1-Lipschitz constraint in Eq. 1, f_{ij} is trained using the WGAN-GP (Gulrajani et al., 2017) with the loss function L ,

$$L = \mathbb{E}_{\mathbf{x}_i \sim \mathbf{y}_i} [f_{ij}(\mathbf{m} \odot \mathbf{x}_i)] - \mathbb{E}_{\mathbf{x}_j \sim \mathbf{y}_j} [f_{ij}(\mathbf{m} \odot \mathbf{x}_j)] + \lambda \mathbb{E}_{\mathbf{r} \sim \mathbf{R}} [\|\nabla_{\mathbf{m} \odot \mathbf{r}} f_{ij}(\mathbf{m} \odot \mathbf{r})\| - 1]^2 \quad (2)$$

where $\mathbf{r} = \epsilon \mathbf{x}_i + (1 - \epsilon) \mathbf{x}_j$, and ϵ is sampled from the uniform distribution in the range of $[0, 1]$ for each step of training, \mathbf{R} is probability distribution of \mathbf{r} . The third term, the gradient penalty, enforces the 1-Lipschitz constraint on f_{ij} by penalizing deviations of the gradient norm from unity along straight lines between samples drawn from \mathbf{y}_i and \mathbf{y}_j . Specifically, the gradient is evaluated with respect to the masked input $\mathbf{m} \odot \mathbf{r}$, ensuring that the Lipschitz constraint is imposed in the masked feature space used for Wasserstein distance estimation. The coefficient λ controls the strength of this regularization.

Algorithm 1 Mask optimization

input Datasets $\{\mathbf{y}_i\}_{i=1}^N$, number of selected residues n , number of random search steps N_{rand} , maximum SA steps N_{SA} , T_{init} , γ , patience $K(= 1000)$
output \mathbf{m}^*

- 1: **Phase 1: Initial random search**
- 2: **for** $b \leftarrow 1$ **to** N_{rand} **do**
- 3: Generate random mask \mathbf{m}_b (with n ones)
- 4: Compute $C(\mathbf{m}_b)$ using Eq. (3)
- 5: **end for**
- 6: $\mathbf{m}_0 \leftarrow \arg \min_{b \in \{1, \dots, N_{\text{rand}}\}} C(\mathbf{m}_b)$
- 7: **Phase 2: Simulated annealing**
- 8: $t \leftarrow 0$, $\mathbf{m}_t \leftarrow \mathbf{m}_0$, $s \leftarrow 0$
- 9: **for** $t \leftarrow 1$ **to** N_{SA} **do**
- 10: $T_t \leftarrow \gamma^t T_{\text{init}}$
- 11: Generate \mathbf{m}_{new} by swapping adjacent 01 \leftrightarrow 10
- 12: Compute $C(\mathbf{m}_{\text{new}})$ using Eq. (3)
- 13: $\Delta C \leftarrow C(\mathbf{m}_{\text{new}}) - C(\mathbf{m}_{t-1})$
- 14: **if** $\Delta C < 0$ **then**
- 15: $\mathbf{m}_t \leftarrow \mathbf{m}_{\text{new}}$
- 16: **else**
- 17: $P_t \leftarrow \exp(-\Delta C/T_t)$ (Eq. (5))
- 18: $u \sim U(0, 1)$
- 19: **if** $u < P_t$ **then**
- 20: $\mathbf{m}_t \leftarrow \mathbf{m}_{\text{new}}$
- 21: **else**
- 22: $\mathbf{m}_t \leftarrow \mathbf{m}_{t-1}$
- 23: **end if**
- 24: **end if**
- 25: **if** $C(\mathbf{m}_t) < \min_{k \in \{0, \dots, t-1\}} C(\mathbf{m}_k)$ **then**
- 26: $s \leftarrow 0$
- 27: **else**
- 28: $s \leftarrow s + 1$
- 29: **end if**
- 30: **if** $s \geq K$ **then**
- 31: **break**
- 32: **end if**
- 33: **end for**
- 34: $\mathcal{M}_{\text{visited}} \leftarrow \{\mathbf{m}_t\}_{t=1}^{N_{\text{SA}}}$
- 35: $\mathbf{m}^* \leftarrow \arg \min_{\mathbf{m} \in \mathcal{M}_{\text{visited}}} C(\mathbf{m})$

3.2. Mask vector optimization for residue selection

Using the neural networks trained to estimate the Wasserstein distance using the random mask, we optimize the binary mask vector. The algorithm for optimizing residue selection consists of two phases based on simulated annealing (Fig. 1c and Algorithm 1).

In Phase 1, we performed the initial random search, in which the promising parameter space of mask vectors is explored using the randomly generated mask vectors (Li & Ma, 2012). Each mask vector is evaluated based on the mask optimiza-

tion cost function C . Since larger Wasserstein distances indicate better discrimination between systems, we define the cost function as the negative sum of the pairwise Wasserstein distances, thereby formulating the optimization as a minimization problem. The cost function C is defined as,

$$C(\mathbf{m}) = - \sum_{i=1}^{N-1} \sum_{i < j}^N W_{ij}(\mathbf{m}) \quad (3)$$

where N is the number of systems, \mathbf{m} is a binary mask vector, and W_{ij} is the Wasserstein distance between system i and j . We randomly generate mask vectors and then select one that minimizes C . The best-performing mask in Phase 1 is then used as the initial binary mask in Phase 2.

In Phase 2, we generate a new mask by swapping neighboring one and zero, that is, "01" is swapped to "10" or vice versa. We evaluated the generated mask using $C(\mathbf{m}_{\text{new}})$, accepting it according to the Metropolis criterion at probability P_t ,

$$\Delta C = C(\mathbf{m}_{\text{new}}) - C(\mathbf{m}_{t-1}), \quad (4)$$

$$P_t = \begin{cases} 1, & \text{if } \Delta C < 0, \\ \exp\left(-\frac{\Delta C}{T_t}\right), & \text{if } \Delta C \geq 0. \end{cases} \quad (5)$$

where t denotes the current optimization step, $C(\mathbf{m}_{t-1})$ and $C(\mathbf{m}_{\text{new}})$ are the cost values for the current and new generated masks, respectively, and T_t is the temperature at step t . The temperature is exponentially decayed as,

$$T_t = \gamma^t T_{\text{init}} \quad (6)$$

where T_{init} is the initial temperature, $\gamma \in (0, 1)$ is the cooling rate.

During simulated annealing, the value of the cost function C is recorded at each step. Rather than selecting the mask obtained at the final iteration, we retain the mask that attains the minimum cost value over the entire optimization trajectory. Specifically, the final selected mask \mathbf{m}^* is defined as

$$\mathbf{m}^* = \arg \min_{\mathbf{m} \in \mathcal{M}_{\text{visited}}} C(\mathbf{m}) \quad (7)$$

Where $\mathcal{M}_{\text{visited}}$ denotes the set of masks explored during simulated annealing. This strategy ensures that the best-performing mask encountered during the search process is used for subsequent analysis.

3.3. Feature extraction from the matrix of Wasserstein distance

After computing the Wasserstein distances for all pairs of systems, we embedded this matrix of Wasserstein distances into the low-dimension space (Fig. 1a). We used non-linear

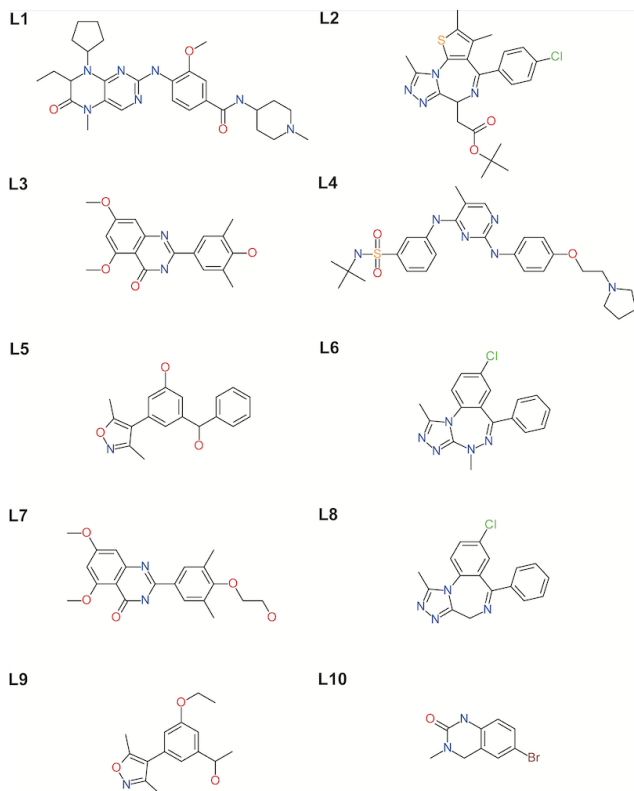


Figure 2. Chemical structure of ligand L1-10

dimension reduction using simulated annealing and the following gradient descent method (Endo et al., 2019; Yasuda et al., 2022). The embedding points are adjusted so that their pairwise Euclidean distance approximates the Wasserstein distances, thus the embedded points are defined as,

$$\{\mathbf{p}_i\}_{i=1}^N = \arg \min_{\{\mathbf{p}_i\}_{i=1}^N} \sum_{1 \leq i < j \leq N} (W_{ij}(\mathbf{m}^*) - \|\mathbf{p}_i - \mathbf{p}_j\|)^2 \quad (8)$$

Subsequently, principal component analysis was performed on the embedded points to ensure rotational invariance.

4. Experiment Settings

4.1. Dataset

To assess the performance of Auto-WHATMD in identifying key residues from MD trajectories of biomolecules, we prepared a dataset of protein–ligand complex systems from a previous study (Yasuda et al., 2022). This dataset contains MD trajectories of BRD4 in both the ligand-free form and 10 different ligand-bound forms (Tab. A1), and the chemical structures of these ligands are shown in Fig. 2. Each system was simulated in three independent unbiased runs for 400 ns. We used the equilibrated trajectories after 50 ns and extracted only the protein atoms. Translation

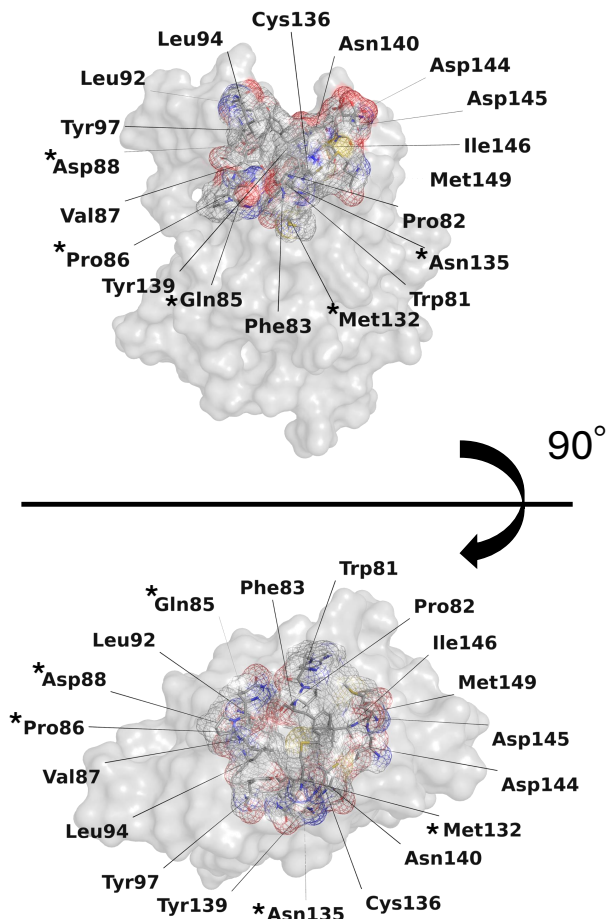


Figure 3. Spatial distribution of residues around the BRD4 binding site. The upper and lower panels show two views rotated by 90°. Residues in the small subset (14 residues) are labeled, and those additionally included in the extended binding-site subset are marked with an asterisk (*).

and rotation were removed from the protein trajectories by aligning the structure on the backbone atoms of 14 residues near the binding site to a reference protein structure (Yasuda et al., 2022). Subsequently, the center of mass of the 14 residues was computed and included in the final dataset. The structure and dynamics of proteins in the dataset exhibit variations due to interactions with the binding ligand. In the previous work (Yasuda et al., 2022), the short-term local dynamics of these 14 residues were suggested to show a pattern related to their ligand-binding free energy.

To examine the robustness of feature selection against changes in the candidate feature space, we further expanded the residue set from 14 to 19 residues by including additional residues surrounding the binding region (Fig. 3). The residues were selected such that any residue with a heavy atom within 6.5 Å of the ligand in more than 50% of the

simulation frames was included. This criterion ensures that the selected residues maintain frequent spatial proximity to the ligand during the trajectory. The same preprocessing procedure, including alignment and trajectory trimming, was applied to the 19-residue setting.

4.2. Neural Network and Optimization

The neural network consisted of two fully connected hidden layers with 2048 units each. The output layer was implemented without bias term. For each predefined mask size n , a separate network was trained. During training, randomly sampled masks were applied at each iteration, and optimization was performed for 5×10^5 iterations.

The Wasserstein distance was approximated using a gradient-penalized formulation with coefficient $\lambda = 10.0$. We used the Adam optimizer with parameters $\beta_1 = 0.0$, $\beta_2 = 0.9$, and $\epsilon = 10^{-3}$. The batch size during training was set to 256, and the learning rate was fixed at $\eta = 1 \times 10^{-4}$. During inference, a larger batch size of 2048 was used to reduce statistical fluctuations in the estimated quantities.

For mask optimization, 10 independent runs with different random seeds were performed with cooling rate $\gamma = 0.999$. Prior to simulated annealing, 10^4 random masks were evaluated, and the mask yielding the lowest objective value was selected as the initial solution. Simulated annealing was conducted using the trained neural network to evaluate the objective function. The initial temperature was determined such that the acceptance probability of typical cost-increasing moves was set to 0.95. To estimate the characteristic magnitude of the cost change ΔC , 1000 random perturbations were evaluated, and the initial temperature was set as

$$T_0 = -\frac{\mathbb{E}[\Delta C]}{\ln(0.95)}. \quad (9)$$

In the simulated annealing procedure, an early-stopping criterion was introduced. The optimization was terminated when no improvement in the cost function was observed for 1000 consecutive steps ($K = 1000$), or when the maximum number of simulated annealing steps ($N_{\text{SA}} = 50000$) was reached.

For low-dimensional embedding, the Wasserstein distance matrix was estimated by averaging the results of the last 1000 forward passes of the trained neural network with a batch size of 2048. The embedding was optimized by minimizing Eq. 8 using simulated annealing followed by gradient-based refinement and setting the dimensionality of p to 3. To obtain a stable solution, 256 independent embedding trials were performed, and the embedding with the lowest objective value was selected as the final result.

5. Results

5.1. Proof-of-concept automatic residue selection

As a representative example, we present the results of auto-WHATMD when selecting four residues from the 14 binding-site residues. In mask optimization, we computed the Wasserstein distance using a neural network trained with randomly sampled masks. While this approach does not rigorously compute the Wasserstein distance during the mask optimization process, we validated its effectiveness by comparing the Wasserstein distances obtained using random masks to those computed using the optimized masks. The random-mask approach yielded Wasserstein distances that correlated well with those from the optimized masks (Fig. A1), supporting the validity of our approximation of the Wasserstein distance.

We first performed experiments to select n residues, for $n = 4$ (Fig. 4a). Ten independent optimization runs were conducted using simulated annealing. Notably, Trp81, Val87, Leu92, and Leu94 were consistently selected in all trials (Fig. 4b), demonstrating high stability and reproducibility of the optimization procedure.

The residues selected by our method are therefore consistent with existing knowledge regarding ligand-induced dynamical modulation. Trp81 has previously been reported by NMR experiments to undergo ligand-induced dynamical changes (Urlick et al., 2016), and its behavior has been suggested to correlate with binding affinity. In addition, Trp81, Val87, and Leu92 have been identified in prior computational and experimental studies as key residues influenced by ligand interactions. Leu92 and Leu94 are located near the hydrophobic binding pocket and are known to contribute to ligand stabilization through hydrophobic contacts (Beier et al., 2024). These residues were identified without incorporating any prior structural or biochemical information.

Using the optimized mask vector (Trp81, Val87, Leu92, Leu94), we recalculated the pairwise Wasserstein distances between systems (Fig. 4c). Relatively large distances were observed between the ligand-unbound system and ligand-bound systems, whereas distances among ligand-bound systems were comparatively small. This pattern suggests that the selected residues effectively capture the dynamical differences associated with ligand binding, while reflecting the similarity among bound states.

To further analyze the global structure of these dynamical differences, the Wasserstein distance matrix was embedded into a two-dimensional space for visualization (Fig. 4d). The ligand-unbound system was clearly separated from the ligand-bound systems. Moreover, the first principal component (PC1) exhibited a monotonic relationship with the ligand binding free energies, indicating that the extracted dynamical feature is strongly associated with binding affin-

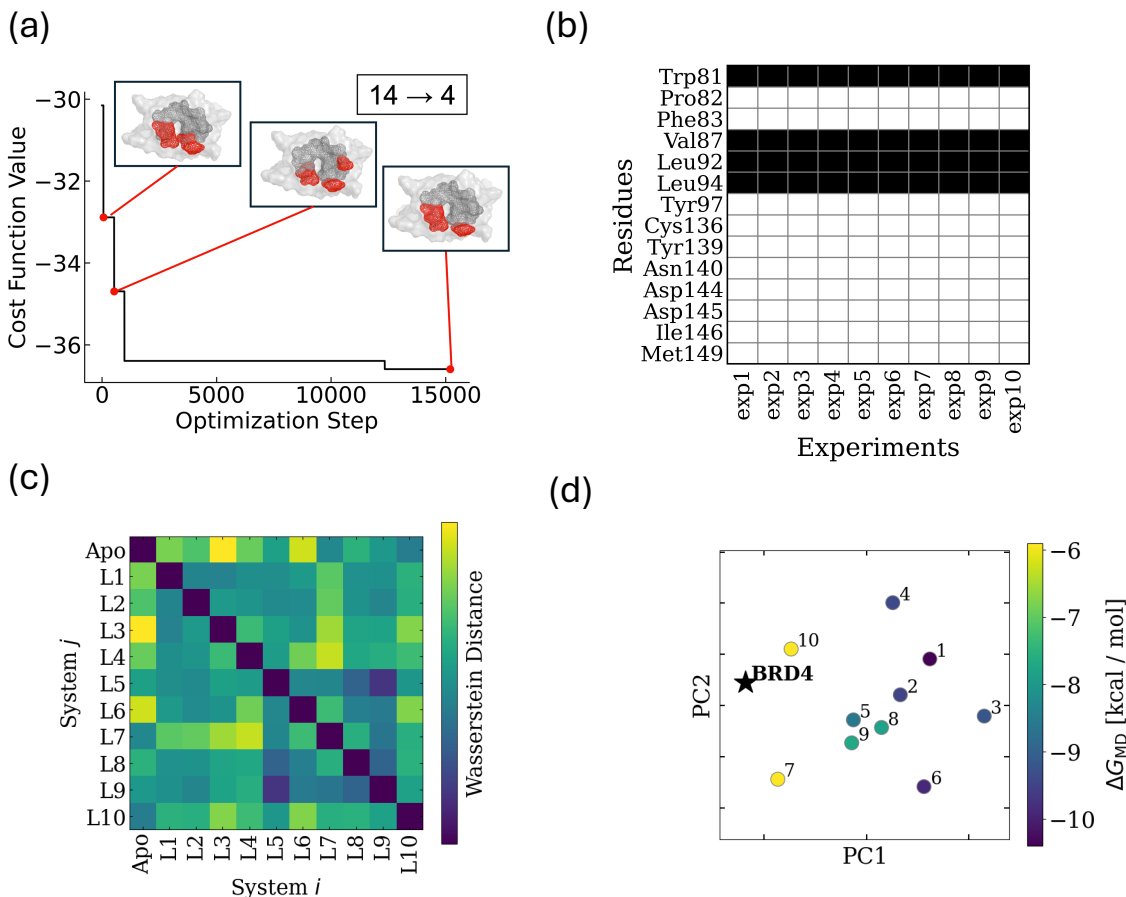


Figure 4. Automatic selection from a small subset in BRD4 systems using auto-WHATMD. (a) Representative process for optimizing residue selection, in which four residues were selected from a subset of 14 residues. Selected residues are shown in red. (b) Residue selection results from ten independent optimization experiments. Selected and non-selected residues are colored in black and white, respectively. (c) Matrix of pairwise Wasserstein distances computed between all systems using the optimized binary mask. Indices correspond to the ligand-free protein (apo) and the 10 ligand-bound systems (L1–L10). (d) Principal component representation of the low-dimensional embedding derived from the Wasserstein distance matrix. Each point represents a system labeled by ligand number. The color indicates the computational ligand-binding free energy ΔG_{MD} reported in Ref. (Aldeghi et al., 2016).

ity.

5.2. Robust residue selection across different subset sizes

We further evaluated the behavior and robustness of the proposed method by (1) varying the number of residue selection in the 14-residues subset, (2) using an extended 19-residues subset. The 19 residues were defined as those exhibiting a contact frequency greater than 0.5 within 6.5 Å of the ligand during the 10 ligand-bound simulations.

For the 14-residues subset, residues located in loop regions, such as Trp81, Val87, and Leu92, were selected when the number of selected residues was small (Fig. 5a). As increasing the number of selected residues, residues around α -helices were also selected. In the 19-residue setting, the selected residue subset partially differed from that obtained using the 14-residue setting. In addition to the previously

identified residues Trp81, Val87, Leu92, and Leu94, the newly included residues located in the ZA loop region, namely Gln85, Val86, and Asp88, tended to be preferentially selected (Fig. 5b).

Auto-WHATMD identified the ZA loop as a key region distinguishing the BRD4 systems, consistent with its known role in ligand recognition (Wu et al., 2021). Previous studies have suggested that the ZA loop exhibits substantial conformational flexibility and can sample a range of conformations, particularly in the apo state, whereas ligand binding tends to restrict its conformational flexibility (Raich et al., 2021; Chen et al., 2022). We compared representative conformations of the ZA-loop region (residues 85–88) (Fig. 6). In the apo system, the ZA loop exhibits relatively flexible behavior and samples a broader region during the simulation. In contrast, in the L3-bound system, the ZA loop

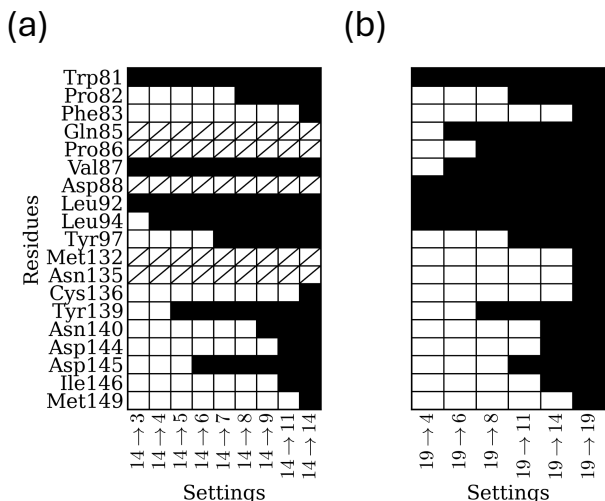


Figure 5. Consistency of selected residues via mask optimization for BRD4 systems. (a) Results for the small subset of 14 residues, varying the number of selected residues from 3 to 14. Residues marked with a crossed line were not included in the subset. Selected and non-selected residues are colored in black and white, respectively. (b) Results for the extended subset of 19 residues around the binding site, varying the number of selected residues from 3 to 19.

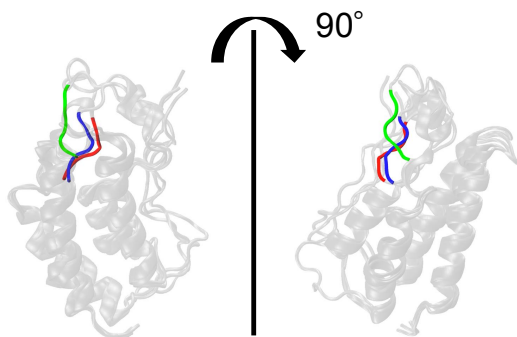


Figure 6. Representative ZA-loop conformations of the apo, L3-bound, and L10-bound systems. The selected residues 85–88 are shown in red (the apo), blue (L3-bound), and green (L10-bound), while other residues are shown as transparent.

remains close to its initial position without large conformational changes. The L10-bound system shows a different behavior from both the apo and L3-bound systems. While the ZA loop initially remains near the starting conformation similarly to the L3-bound system, it later adopts a conformation that is distinct from those observed in the apo and L3-bound trajectories, as illustrated in Fig. 6. These results indicate that auto-WHATMD detected differences of the ZA loop conformations.

5.3. Relationship between a feature of selected residues and ligand-binding free energy

As a measurement criterion of the embedding, we calculated Pearson’s correlation coefficient between PC1 and the ligand binding energies. The ligand binding energies are an important indicator of the stability of protein–ligand complexes and range from -10.4 to -5.9 kcal/mol in this dataset, as reported in previous free energy calculations using MD simulations (Aldeghi et al., 2016) (Tab. A1).

Using the 14-residues subset, the correlation to G_{MD} ranged from 0.77–0.94, depending on the number of selected residues (Fig. 7; see also Figs. A2 and A3 for the corresponding two-dimensional embeddings in the PC1–PC2 space and PC1– ΔG plots, respectively). The highest correlation with G_{MD} was observed at $n = 6$. Similarly, the correlation with G_{EXP} ranged from 0.54–0.73 (Fig. 7). We note that the lower performance with G_{EXP} may be attributed to the limited accuracy of the force field parameters and insufficient sampling in the MD simulations. Overall, these results suggest that the low-dimensional embedding obtained by the proposed method successfully extracts essential features associated with ligand binding.

The data representations between the 14- and 19-residues subsets differ slightly due to differences in the fitting references, but we then demonstrate that this fitting effect does not significantly effect PC1– ΔG correlation. For the 19-residues site, the Pearson correlation coefficient with ΔG_{MD} ranged from 0.81–0.88, while the correlation with ΔG_{EXP} ranged from 0.61–0.74 (Fig. 7). These results indicate that high correlation values were preserved in the extended subset.

6. Limitations

Although we have demonstrated that auto-WHATMD robustly selected key residues and that the feature based on the selected residues can dictate the ligand-binding properties, there are several limitations. First, we used the positions in the xyz coordinate as inputs to represent the dynamics in three dimensional space, rather than commonly used features such as distance or angles as the input. We aligned all systems to a subset of residues in the reference structure to ensure translational and rotational invariance. However, selecting reference residues is more challenging for flexible loops or when all residues of a protein are included as input, highlighting the need for improved residue representation. Second, our neural networks are trained separately for each pair of systems. Applying them to additional systems requires re-training the model for the new system pair. Finally, our unsupervised learning framework does not ensure matching to the binding affinity. Combining the method with other features such as docking scores could increase the

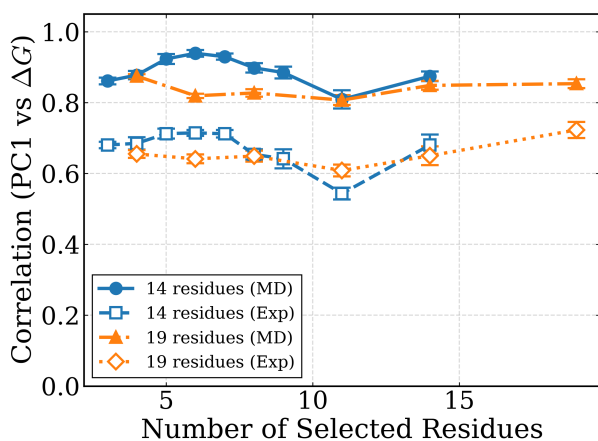


Figure 7. Correlation between ligand-binding free energy and the PC1 extracted from the Wasserstein distance matrix. Absolute Pearson correlation coefficients between PC1 and ligand-binding free energy (ΔG_{MD} or ΔG_{EXP}) are shown as a function of the number of selected residues for the 14- and 19-residue subsets. Solid lines represent correlations with ΔG_{MD} , and dashed/dotted lines with ΔG_{EXP} .

interpretability of the obtained features (Igarashi & Ohue, 2025).

7. Conclusion

We have presented auto-WHATMD, an algorithm for representing differences among multiple molecular dynamics trajectories. Applying it to BRD4 protein systems, we demonstrated that auto-WHATMD identified biologically important residues. The selection was robust regardless of the size of the candidate residue subset and the number of selected residues, ensuring consistent representation of system differences. Moreover, the PC1 derived from auto-WHATMD correlated with ligand-binding free energies.

We believe that auto-WHATMD effectively addresses the challenges associated with comparing ensembles. Protein dynamics are highly sensitive to various factors, such as ligand binding, temperature changes, and solvent types, which is a currently focused research area driven by extensive MD simulations. Auto-WHATMD could effectively characterize the differences between these systems, providing valuable biological insights into protein behavior.

References

Aldeghi, M., Heifetz, A., Bodkin, M. J., Knapp, S., and Biggin, P. C. Accurate calculation of the absolute free energy of binding for drug molecules. *Chemical Science*, 7(1):207–218, 2016.

Arjovsky, M., Chintala, S., and Bottou, L. Wasserstein gan.

arXiv preprint, arXiv:1701.07875v3, 2017.

- Baek, M., DiMaio, F., Anishchenko, I., Dauparas, J., Ovchinnikov, S., Lee, G. R., Wang, J., Cong, Q., Kinch, L. N., Schaeffer, R. D., et al. Accurate prediction of protein structures and interactions using a three-track neural network. *Science*, 373(6557):871–876, 2021.
- Beier, A., Platzer, G., Höfurtherner, T., Ptaszek, A. L., Lichtenacker, R. J., Geist, L., Fuchs, J. E., McConnell, D. B., Mayer, M., and Konrat, R. Probing protein-ligand methyl- π interaction geometries through chemical shift measurements of selectively labeled methyl groups. *Journal of Medicinal Chemistry*, 67(15):13187–13196, 2024. doi: 10.1021/acs.jmedchem.4c01128.
- Bottaro, S. and Lindorff-Larsen, K. Biophysical experiments and biomolecular simulations: A perfect match? *Science*, 361(6400):355–360, 2018.
- Brüschweiler, R. Efficient rmsd measures for the comparison of two molecular ensembles. *Proteins: Structure, Function, and Bioinformatics*, 50(1):26–34, 2003.
- Chen, S., He, Y., Geng, Y., Wang, Z., Han, L., and Han, W. Molecular dynamic simulations of bromodomain and extra-terminal protein 4 bonded to potent inhibitors. *Molecules*, 27(1):118, 2022.
- Ciceri, P., Müller, S., O’mahony, A., Fedorov, O., Filippakopoulos, P., Hunt, J. P., Lasater, E. A., Pallares, G., Picaud, S., Wells, C., et al. Dual kinase-bromodomain inhibitors for rationally designed polypharmacology. *Nature Chemical Biology*, 10(4):305–312, 2014.
- Endo, K., Tomobe, K., and Yasuoka, K. Multi-step time series generator for molecular dynamics. In *Proceedings of the AAAI Conference on Artificial Intelligence*, volume 32, 2018.
- Endo, K., Yuhara, D., Tomobe, K., and Yasuoka, K. Detection of molecular behavior that characterizes systems using a deep learning approach. *Nanoscale*, 11(20):10064–10071, 2019.
- Filippakopoulos, P., Qi, J., Picaud, S., Shen, Y., Smith, W. B., Fedorov, O., Morse, E. M., Keates, T., Hickman, T. T., Felletar, I., et al. Selective inhibition of bet bromodomains. *Nature*, 468(7327):1067–1073, 2010.
- Filippakopoulos, P., Picaud, S., Fedorov, O., Keller, M., Wrobel, M., Morgenstern, O., Bracher, F., and Knapp, S. Benzodiazepines and benzotriazepines as protein interaction inhibitors targeting bromodomains of the bet family. *Bioorganic & Medicinal Chemistry*, 20(6):1878–1886, 2012.

- Fish, P. V., Filippakopoulos, P., Bish, G., Brennan, P. E., Bunnage, M. E., Cook, A. S., Federov, O., Gerstenberger, B. S., Jones, H., Knapp, S., et al. Identification of a chemical probe for bromo and extra c-terminal bromodomain inhibition through optimization of a fragment-derived hit. *Journal of Medicinal Chemistry*, 55(22):9831–9837, 2012.
- Glielmo, A., Husic, B. E., Rodriguez, A., Clementi, C., Noé, F., and Laio, A. Unsupervised learning methods for molecular simulation data. *Chemical Reviews*, 121(16):9722–9758, 2021.
- González-Delgado, J., Sagar, A., Zanon, C., Lindorff-Larsen, K., Bernadó, P., Neuvial, P., and Cortés, J. Wasco: a wasserstein-based statistical tool to compare conformational ensembles of intrinsically disordered proteins. *Journal of Molecular Biology*, 435(14):168053, 2023.
- Gulrajani, I., Ahmed, F., Arjovsky, M., Dumoulin, V., and Courville, A. C. Improved training of wasserstein gans. *Advances in Neural Information Processing Systems*, 30, 2017.
- Henzler-Wildman, K. and Kern, D. Dynamic personalities of proteins. *Nature*, 450(7172):964–972, 2007.
- Hewings, D. S., Fedorov, O., Filippakopoulos, P., Martin, S., Picaud, S., Tumber, A., Wells, C., Olcina, M. M., Freeman, K., Gill, A., et al. Optimization of 3, 5-dimethylisoxazole derivatives as potent bromodomain ligands. *Journal of Medicinal Chemistry*, 56(8):3217–3227, 2013.
- Igarashi, K. and Ohue, M. Protein–ligand affinity prediction via jensen-shannon divergence of molecular dynamics simulation trajectories. *Biophysics and Physicobiology*, 22(3):e220015, 2025.
- Janson, G., Valdes-Garcia, G., Heo, L., and Feig, M. Direct generation of protein conformational ensembles via machine learning. *Nature Communications*, 14(1):774, 2023.
- Jumper, J., Evans, R., Pritzel, A., Green, T., Figurnov, M., Ronneberger, O., Tunyasuvunakool, K., Bates, R., Žídek, A., Potapenko, A., et al. Highly accurate protein structure prediction with alphafold. *Nature*, 596(7873):583–589, 2021.
- Karplus, M. and Kuriyan, J. Molecular dynamics and protein function. *Proceedings of the National Academy of Sciences*, 102(19):6679–6685, 2005.
- Lemke, T. and Peter, C. Encodermap: Dimensionality reduction and generation of molecule conformations. *Journal of Chemical Theory and Computation*, 15(2):1209–1215, 2019.
- Lewis, S., Hempel, T., Jiménez-Luna, J., Gastegger, M., Xie, Y., Foong, A. Y. K., Satorras, V. G., Abdin, O., Veeling, B. S., Zaporozhets, I., Chen, Y., Yang, S., Schneuing, A., Nigam, J., Barbero, F., Stimper, V., Campbell, A., Yim, J., Lienen, M., Shi, Y., Zheng, S., Schulz, H., Munir, U., Clementi, C., and Noé, F. Scalable emulation of protein equilibrium ensembles with generative deep learning. *bioRxiv*, 2024. doi: 10.1101/2024.12.05.626885.
- Lewis, S., Hempel, T., Jiménez-Luna, J., Gastegger, M., Xie, Y., Foong, A. Y., Satorras, V. G., Abdin, O., Veeling, B. S., Zaporozhets, I., et al. Scalable emulation of protein equilibrium ensembles with generative deep learning. *Science*, 389(6761):eadv9817, 2025.
- Li, X. and Ma, L. Minimizing binary functions with simulated annealing algorithm with applications to binary tomography. *Computer Physics Communications*, 183(2):309–315, 2012.
- Lindorff-Larsen, K. and Ferkinghoff-Borg, J. Similarity measures for protein ensembles. *PLoS One*, 4(1):e4203, 2009.
- Lindorff-Larsen, K., Piana, S., Dror, R. O., and Shaw, D. E. How fast-folding proteins fold. *Science*, 334(6055):517–520, 2011.
- Lu, W., Zhang, J., Huang, W., Zhang, Z., Jia, X., Wang, Z., Shi, L., Li, C., Wolynes, P. G., and Zheng, S. Dynamicbind: Predicting ligand-specific protein-ligand complex structure with a deep equivariant generative model. *Nature Communications*, 15(1):1071, 2024.
- Mardt, A., Pasquali, L., Wu, H., and Noé, F. Vampnets for deep learning of molecular kinetics. *Nature Communications*, 9(1):5, 2018.
- Mustali, J., Yasuda, I., Hirano, Y., Yasuoka, K., Gautieri, A., and Arai, N. Unsupervised deep learning for molecular dynamics simulations: a novel analysis of protein–ligand interactions in sars-cov-2 m pro. *RSC Advances*, 13(48):34249–34261, 2023.
- Noé, F., Olsson, S., Köhler, J., and Wu, H. Boltzmann generators: Sampling equilibrium states of many-body systems with deep learning. *Science*, 365(6457):eaaw1147, 2019.
- Picaud, S., Wells, C., Felletar, I., Brotherton, D., Martin, S., Savitsky, P., Diez-Dacal, B., Philpott, M., Bountra, C., Lingard, H., et al. Rvx-208, an inhibitor of bet transcriptional regulators with selectivity for the second bromodomain. *Proceedings of the National Academy of Sciences*, 110(49):19754–19759, 2013.
- Plattner, N. and Noé, F. Protein conformational plasticity and complex ligand-binding kinetics explored by atomistic simulations and markov models. *Nature Communications*, 6(1):7653, 2015.

-
- Raich, L., Meier, K., Günther, J., Christ, C. D., Noé, F., and Olsson, S. Discovery of a hidden transient state in all bromodomain families. *Proceedings of the National Academy of Sciences*, 118(39):e2104443118, 2021.
- Tiberti, M., Papaleo, E., Bengtsen, T., Boomsma, W., and Lindorff-Larsen, K. Encore: software for quantitative ensemble comparison. *PLoS Computational Biology*, 11(10):e1004415, 2015.
- Urlick, A. K., Calle, L. P., Espinosa, J. F., Hu, H., and Pomerantz, W. C. Protein-observed fluorine nmr is a complementary ligand discovery method to 1h cpmg ligand-observed nmr. *ACS Chemical Biology*, 11(11): 3154–3164, 2016.
- Van Der Lee, R., Buljan, M., Lang, B., Weatheritt, R. J., Daughdrill, G. W., Dunker, A. K., Fuxreiter, M., Gough, J., Gsponer, J., Jones, D. T., et al. Classification of intrinsically disordered regions and proteins. *Chemical Reviews*, 114(13), 2014.
- Villani, C. et al. *Optimal transport: old and new*, volume 338. Springer, 2009.
- Vögele, M., Thomson, N. J., Truong, S. T., McAvity, J., Zachariae, U., and Dror, R. O. Systematic analysis of biomolecular conformational ensembles with pensa. *The Journal of Chemical Physics*, 162(1), 2025.
- Wu, S., Wang, L., Zhang, L., Xu, X., and Zhao, J. Molecular dynamics insights into binding selectivity of inhibitors toward brd4 and cbp. *Chemical Physics Letters*, 769: 138435, 2021.
- Yasuda, I., Endo, K., Yamamoto, E., Hirano, Y., and Yasuoka, K. Differences in ligand-induced protein dynamics extracted from an unsupervised deep learning approach correlate with protein–ligand binding affinities. *Communications Biology*, 5(1):481, 2022.

Appendix

L	ΔG_{MD}	ΔG_{EXP}	PDB ID	Ref ΔG_{EXP}
1	-10.4	-9.8	4OGI	(Ciceri et al., 2014)
2	-9.5	-9.6	3MXF	(Filippakopoulos et al., 2010)
3	-9.2	-9.0	4MR3	(Picaud et al., 2013)
4	-9.4	-8.9	4OGJ	(Ciceri et al., 2014)
5	-8.6	-8.8	4J0R	(Hewings et al., 2013)
6	-9.9	-8.2	3U5L	(Filippakopoulos et al., 2012)
7	-5.9	-7.8	4MR4	(Picaud et al., 2013)
8	-7.8	-7.4	3U5J	(Filippakopoulos et al., 2012)
9	-7.7	-7.3	3SVG	(Picaud et al., 2013)
10	-5.9	-6.3	4HBV	(Fish et al., 2012)

Table A1. Calculated and experimental ΔG in kcal/mol values used in the dataset of BRD4 simulations. ΔG_{MD} is obtained from (Aldeghi et al., 2016).

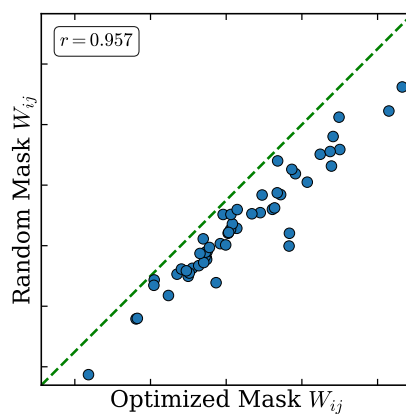


Figure A1. Comparison of the Wasserstein distance of all 55 pairs from the BRD4 systems, computed using neural networks trained with random masks (Random mask W_{ij}) and neural networks re-trained with the mask optimized for five-residues selection (Optimized mask W_{ij}). For optimized masks W_{ij} , the neural networks are initialized and re-trained for 500,000 steps. Green dashed line shows $y = x$.

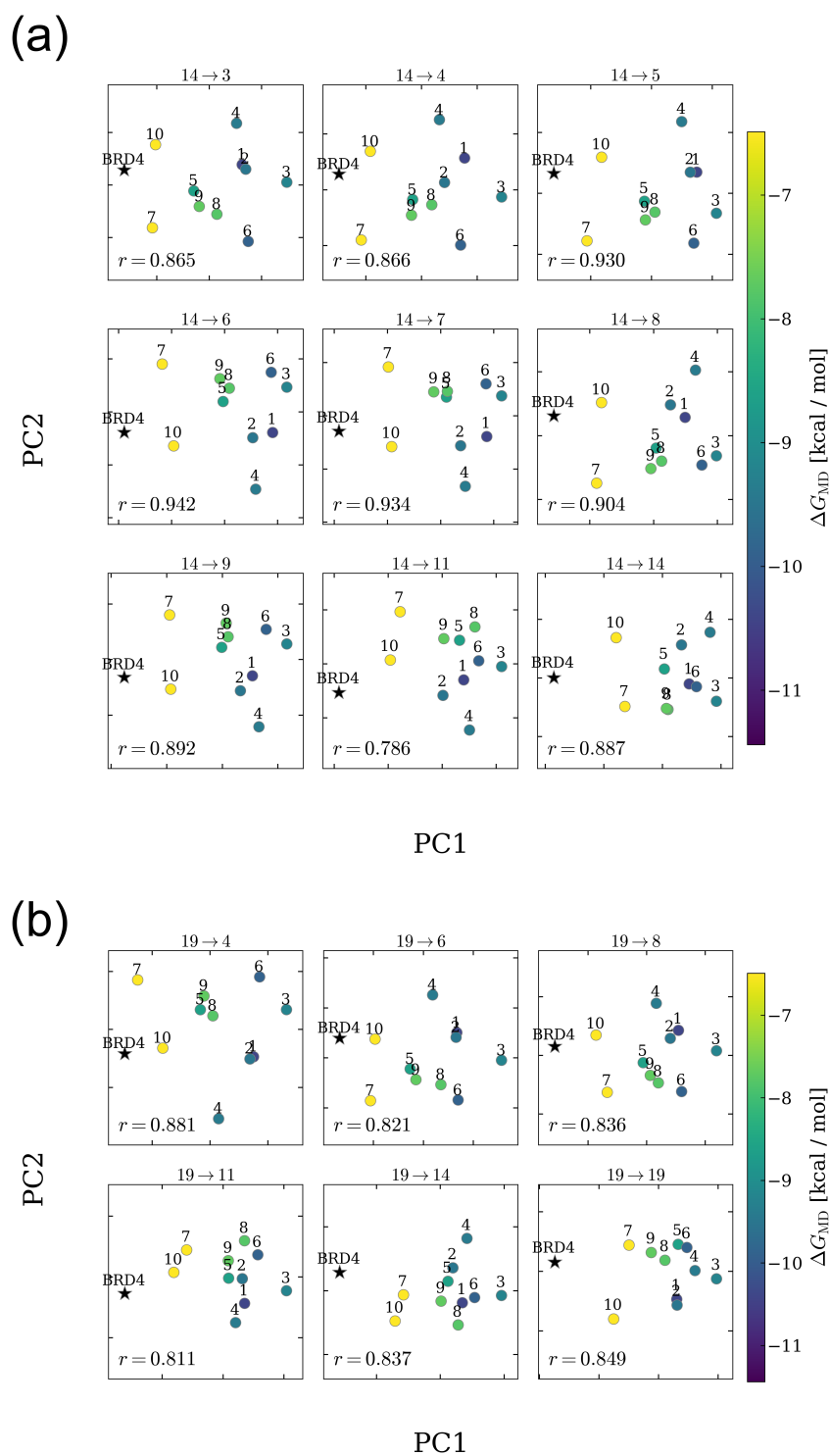


Figure A2. Two-dimensional embeddings of the BRD4 systems obtained from Wasserstein distance matrices computed from the selected residue subsets. The color of each point represents the binding free energy obtained from (Aldeghi et al., 2016). (a) Results for the 14-residue candidate set, where the number of selected residues was varied from 3 to 14. (b) Results for the extended 19-residue candidate set around the binding site, where the number of selected residues was varied from 4 to 19.

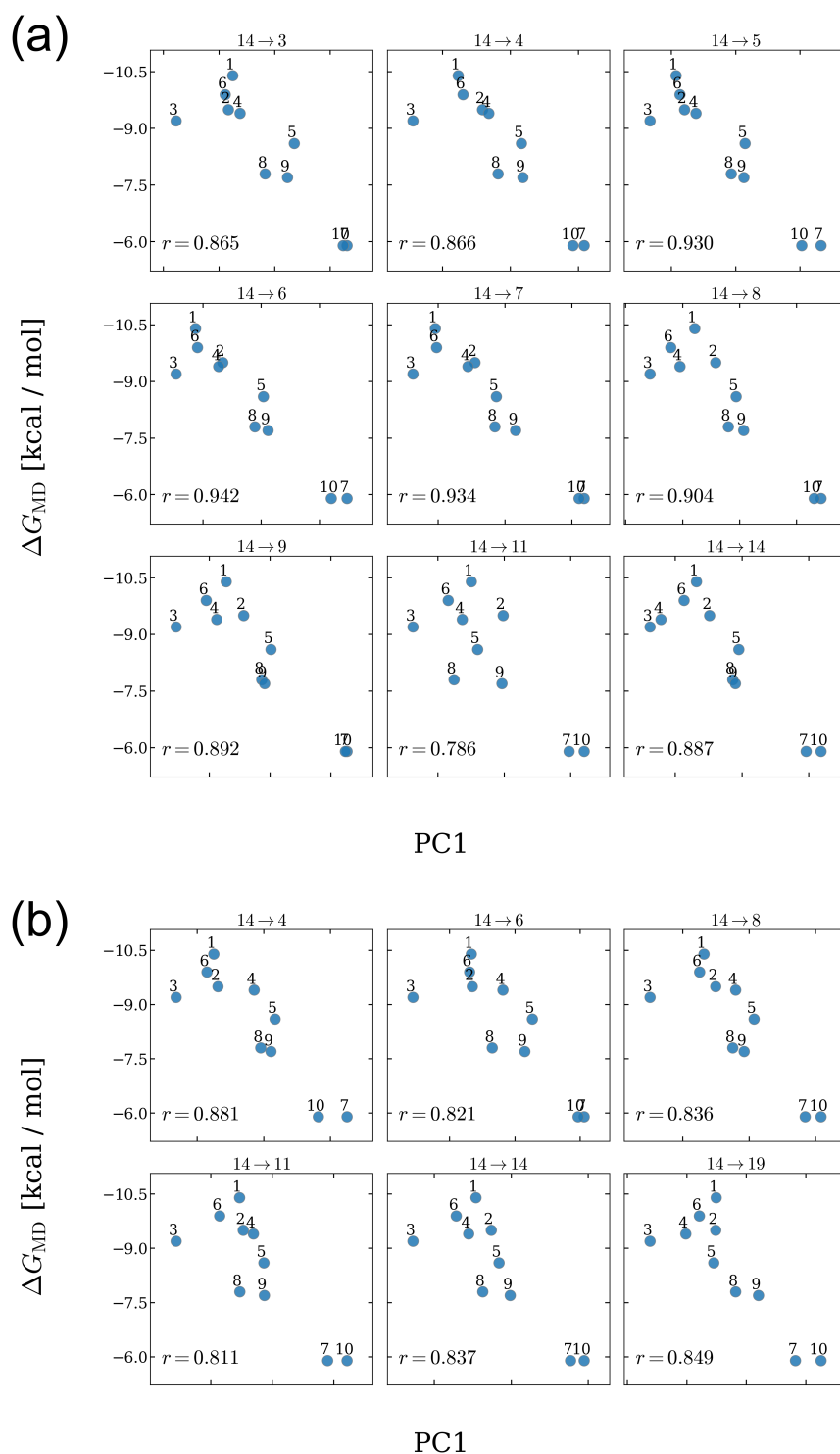


Figure A3. Plots of PC1 from auto-WHATMD with the binding free energy ΔG_{MD} (Aldeghi et al., 2016) for the BRD4 systems. The numbers attached to the points indicate the ligand labels. (a) Results for the 14-residue candidate set, where the number of selected residues was varied from 3 to 14. (b) Results for the extended 19-residue candidate set around the binding site, where the number of selected residues was varied from 4 to 19.